

Protein Transport to Choroid and Retina following Periocular Injection: Theoretical and Experimental Study

FEILIM MAC GABHANN,¹ ANNA MARIA DEMETRIADES,² TYE DEERING,² JONATHAN D. PACKER,¹ SYED MAHMOOD SHAH,² ELIA DUH,² PETER A. CAMPOCHIARO,² and ALEKSANDER S. POPEL¹

¹Department of Biomedical Engineering; and ²The Wilmer Eye Institute, Johns Hopkins University School of Medicine, Baltimore, MD USA

(Received 20 July 2005; accepted 16 November 2006; published online 3 February 2007)

Abstract—Ocular neovascularization is a major cause of blindness in several diseases including age-related macular degeneration (choroidal neovascularization) and diabetic retinopathy (retinal neovascularization). Antiangiogenic agents with clinically significant effects exist, but a key question remains: how to effectively deliver drugs to the site of neovascularization. Periocular delivery of drugs or proteins is less invasive and safer than intravitreal delivery, but little is known regarding how and to what extent agents access intraocular tissues after periocular injection. We present a computational model of drug or protein transport into the eye following periocular injection to quantify movement of macromolecules across the sclera of the mouse eye. We apply this model to the movement of green fluorescent protein (GFP) across the mouse eye and fit the results of *in vivo* experiments to find transport parameters. Using these parameters, the model gives the profile of interstitial GFP concentration across the sclera, choroid and retina. We compare this to predictions of transport following intravitreal injections. We then scale up the model to estimate the transport of GFP into the human choroid and retina; the thicker sclera decreases transscleral delivery. This is the first model of ocular drug delivery to explicitly account for transport properties of each eye layer.

Keywords—Drug delivery, Mathematical model, Angiogenesis, Anti-angiogenic drug, Green fluorescent protein, Diffusion.

INTRODUCTION

Ocular neovascularization is a major cause of irreversible vision loss. In patients with age-related macular degeneration, new vessels sprout from choroidal vessels, grow through Bruch's membrane, and invade

the retinal pigmented epithelial (RPE) cell layer and the retina. The new vessels leak and bleed resulting in collection of blood and fluid beneath and within the retina causing reversible loss of vision, but over time scarring occurs resulting in permanent loss of vision.⁸ In patients with diabetic retinopathy, new vessels sprout from retinal vessels, grow through the internal limiting membrane into the vitreous cavity where they leak and bleed to cause reversible loss of vision. Over time the new vessels recruit other cells resulting in scarring on the surface of the retina, which can pull on the retina and detach it resulting in severe and potentially permanent loss of vision unless the problem is corrected by surgery.

Over the past several years, significant progress has been made elucidating the molecular pathogenesis of ocular neovascularization. Several lines of evidence have indicated that vascular endothelial growth factor (VEGF) is a critical stimulus for both retinal and choroidal neovascularization. The identification of this molecular target has led to several strategies to inhibit it. Intravitreal injections of an aptamer that binds VEGF slow the rate of vision loss in patients with neovascularization and is now part of standard care.¹⁶ Intravitreal injection of an antibody fragment that binds VEGF has been shown to provide benefit in patients with choroidal neovascularization due to AMD and is currently in phase III trials.³¹ Intravitreal injections result in high intraocular levels of therapeutic agents, but can result in serious sight-threatening complications including endophthalmitis (infection within the eye) and retinal detachment. Development of alternative routes of delivery of therapeutic agents to the choroid and retina would be useful.

Periocular delivery entails deposition of drugs or proteins beneath the conjunctiva against the external surface of the sclera. Since the eye wall is not violated, there is little risk of endophthalmitis or retinal

Address correspondence to Feilim Mac Gabhann, Department of Biomedical Engineering, Johns Hopkins University School of Medicine, 720 Rutland Ave, #613 Traylor, Baltimore, MD 21205, USA. Electronic mail: feilim@jhu.edu

detachment. Several lines of evidence have suggested that this delivery approach may be feasible for some proteins,^{13,14,33} but it is difficult to predict how a protein is likely to behave, because the mechanism by which they enter the eye from the periocular space is poorly understood. In this study, we developed a model for transscleral delivery of proteins and tested the model by measuring green fluorescent protein (GFP) levels in ocular tissues at several time points after periocular injections of GFP. We selected GFP, because it is a relatively small (27 kD) protein that is completely foreign to mice and is unlikely to have any specific binding sites in ocular tissue that could complicate the analysis.

Having characterized the transport of GFP, we predict the transport of the same protein following intravitreal injection. We also scale up the model to predict transport of drug for a similar periocular injection protocol in the human eye. Our model is the first that describes local ocular drug delivery and accounts explicitly for each of the layers of the eye from the periocular tissue to the vitreous. The model focuses on proteins, not on small molecule drugs, which have significantly lower molecular weight and resistance to transport. Proteins that could be useful as angiostatic agents include antibodies to angiogenic stimulators, soluble (non-membrane bound) isoforms of the receptor for angiogenic promoters, and endogenous angiostatic agents, e.g. endostatin and pigment epithelium-derived factor (PEDF).

METHODS

Measurement of Scleral and Choroidal Thickness in Mouse Eyes

Healthy 6–8 weeks old C57BL/6 mice were euthanized and eyes were frozen in optimal cutting temperature (OCT) embedding medium. Ten sections through the optic disc of each eye were fixed, stained and analyzed under 20x magnification with Image Pro Plus software (MediaCybernetics, Silver Spring, MD). Sclera and retinal pigmented epithelium (RPE)/choroid layers were identified and the area and length of segments of these layers measured in well-preserved specimens to determine the average thickness of the layers. Thickness was analyzed close to the optic disk, at the equator of the eye and at intermediate points.

Measurement of Retinal Thickness in Mouse Eyes

Eyes of healthy 6–8 weeks old C57BL/6 mice were prepared as above. Retinal thickness was obtained using StratusOCT (Carl Zeiss Meditec, Dublin, CA). The optic disc was identified using built-in fundus

camera and real time optical cross sections. Using a modified fast macular thickness acquisition protocol, multiple cross sections were obtained in the area around the disc. Retinal thickness was measured using retinal thickness map algorithm. Scan line profiling was done for correction of automated maps where necessary. The results were compared to the thickness of retina in H&E stained histological sections analyzed using Image Pro Plus software (MediaCybernetics, Silver Spring, MD).

Periocular Injections and GFP Concentration Measurements

Adult female C57BL/6 mice were anesthetized and injected, in the subconjunctival space of one eye, with 5 μ l of a solution containing 3.65 μ g recombinant GFP (Roche Applied Science, Indianapolis, IN); there was no injection in contralateral eye. Mice were euthanized at multiple timepoints, and eyes were removed. The corneas and lenses were removed, and sclera, choroid, and retina were isolated. Under a dissecting microscope, the retina was gently elevated from the RPE, severed at the optic nerve, removed from the eye and placed in homogenization buffer. The RPE and choroid were scraped from the sclera and placed in buffer. The remaining sclera was placed in buffer and each of the isolated tissues were homogenized in 200 μ l 0.01% Triton X-100 with Complete Mini protease inhibitors (Roche Applied Science, Indianapolis, IN) and microfuged. Total protein concentration in the supernatants was measured by Bio-Rad protein assay (Bio-Rad, Hercules, CA) and GFP concentration was measured by a sandwich ELISA (Pierce, Rockford, IL) using rabbit anti-GFP IgG (Molecular Probes, Eugene, OR) and goat anti-rabbit IgG (Sigma, St. Louis, MO).

Although GFP is a fluorescent protein, we did not use fluorescent images to track the transport of GFP through the tissue layers. Each layer has different structural characteristics and may have a different relationship between fluorescent intensity and actual GFP concentration. The use of an ELISA assay on the homogenized tissue enables a quantitative comparison of the absolute concentrations of GFP in the sclera, choroid and retina.

Recombinant proteins were used to generate standard curves. The standard curves were used to determine the concentration of the protein of interest in samples. Concentrations are reported as ng GFP/ μ g protein; to compare with the results of the model, we converted this to moles GFP/L tissue, assuming 3% w/v as the protein content of the tissue.¹⁰ Control eyes were used to subtract background or non-specific GFP antibody binding. All mice were treated humanely in

strict compliance with the Association for Research in Vision and Ophthalmology statement on the use of animals in research. The protocol for this study was approved by the Animal Care and Use Committee of the Johns Hopkins University School of Medicine.

Initial concentration of GFP

The injected solution contained 3.65 μg GFP in 5 μl . GFP has a molecular weight of 27 kDa and so the initial GFP concentration in the episcleral space was 27 μM . GFP is not produced by the mouse, so the initial concentration elsewhere in the eye was zero.

Spread of Injected Solution around the Globe of the Eye

The radius of the mouse eye is approximately 1.5 mm, giving an outer surface area of 0.28 cm^2 . The sclera covers 92% of the human eye²⁵ and 87–89% of the porcine eye;²⁷ we assume it covers five-sixths of the mouse eye. To determine the spread of a 5 μl injectate in the periocular space, 5 μl of ink was injected in three mouse eyes and the area of sclera stained by the ink was measured to be $68.5 \pm 16\%$, or 58% coverage of the entire globe, and thus the mean thickness of the potential space occupied by the 5 μl injected fluid is 310 μm .

Transport Through the Layers of the Eye

In our model, the eye is considered to have five layers (see Fig. 1b). We neglect transport around the eye, and thus developed a one-dimensional model of radial movement through the layers. We do not expect a 2d or 3d model to yield improved agreement with the

results or improved insight, as the experimental tissue layers are homogenized upon extractions.

Each layer is characterized by unique transport characteristics: diffusivity, D_i , and void fraction, ϕ_i . A lumped parameter (compartmental) model was considered but not used as this would have increased the unknown parameters as known diffusivities were subsumed into unknown resistances between layers. The void fraction in this case is that fraction of the tissue occupied by interstitial (extracellular, but nonvascular) space through which GFP diffuses. Intravascular and intracellular spaces reduce the void fraction of the tissue, as do dense extracellular structures.

The episcleral space is assumed to contain no cells and is modeled as an aqueous environment because GFP was injected in aqueous buffer. GFP injected into the periocular space diffuses in two directions: away from the eye into the systemic circulation and through the sclera, choroid and retina into the vitreous. The sclera is an avascular and largely acellular coat of extracellular matrix that gives the eye its strength and shape. The sclera is not thought to be a significant diffusive barrier, and the permeability of sclera of various animal species has been measured in vitro.^{2,3,21} The surface area of the sclera is large, its permeability does not decline with age²⁶ and particles up to 100 nm radius have been shown to diffuse through the sclera.¹⁷

The choroid consists of a dense network of large and small blood vessels and a relatively sparse population of fibroblasts and melanocytes. Bruch’s membrane is an acellular extracellular matrix structure that provides support for the monolayer of RPE cells that is located on its inner surface. The retina consists of several layers of densely packed neuronal and glial cells; the inner 2/3 of the retina is vascularized. The

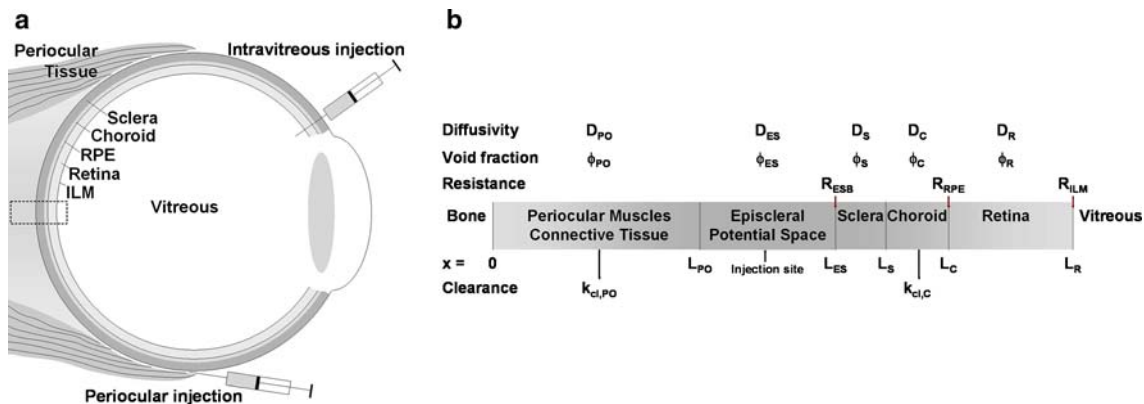


FIGURE 1. Geometry of the mouse eye. a, Globe of the eye showing the layers of the posterior segment of the eye, and intravitreal and periocular injection sites. b, Schematic of the layers of the posterior segment of the eye. The periocular injection site is an episcleral potential space. ESB, episcleral barrier; RPE, retinal pigmented epithelium; BM, Bruch’s Membrane; ILM, internal limiting membrane.

inner surface of the retina is separated from the vitreous by the internal limiting membrane (ILM).

Each layer provides some resistance to diffusion, but two regions thought to exhibit high resistance are the RPE-Bruch's membrane complex, which provides a molecular-size-dependent barrier to transport between the choroid and retina, and the ILM, which is a barrier between the retina and the vitreous. There may in addition be a resistance at the episcleral barrier (Fig. 1b).

The interstitial concentration is the local concentration in the layers of the eye. This is the concentration available to be sensed by cells and other molecules, and is thus assumed to be crucial to therapeutic benefits of drug delivery. However, the concentration measured by experiment after excision of the tissues is an effective concentration (g GFP/g total protein) due to the homogenization of the tissue. If we assume the total protein concentration of each tissue to be similar (extracellular plus cellular protein) then the effective concentration measured for each layer is proportional to the interstitial concentration of GFP adjusted for the extracellular volume fraction (as cells exclude the diffusing protein but are included in the homogenized tissue). The partial coverage of the globe also plays a role in the effective concentration (although we assume here the same coverage for each of the layers). Thus the effective (measured) concentration, C , is equivalent to

$$C = C_{\text{int}}\phi_i\alpha \quad (1)$$

where C_{int} is the interstitial concentration, ϕ_i is the void fraction and α is the fractional coverage of the sclera. The concentration in each layer is governed by diffusion and clearance. There may also be binding to cell surface receptors or extracellular matrix binding sites, but for GFP we ignore binding as no known receptors exist in the mouse or human. Thus, the governing equation is:

$$\frac{\partial C_i}{\partial t} = D_i \frac{\partial^2 C_i}{\partial x^2} - k_{\text{cl},i} C_i \quad (2)$$

where C_i is the effective concentration, D_i the diffusivity, and $k_{\text{cl},i}$ the clearance rate of GFP in layer i .

For each layer we impose two boundary conditions, ten in all. The periorcular tissues have a zero-flux condition at the muscle-bone interface; the other conditions are local concentration balances

$$C_i(L_i) - \phi_{ij} C_j(L_i) = -D_i R_{ij} \frac{\partial C_i}{\partial x}(L_i) \quad (3)$$

and flux balances

$$D_i \frac{\partial C_i}{\partial x}(L_i) = D_j \frac{\partial C_j}{\partial x}(L_i) \quad (4)$$

where the partition coefficients ϕ_{ij} are ratios of void fractions, $\phi_{ij} = \phi_i/\phi_j$; L_i is the spatial position (see Fig. 1b), and R_{ij} the resistance of the barrier between layers i and j .

The vitreous is assumed to be a large sink and to have effectively zero concentration of the marker molecule for the short times investigated here. The initial distribution of the molecule is taken to be zero everywhere except in the periorcular space, where the concentration is that of the initial injection, C_0

$$C_i(x, t = 0) = f(x) = [H(x - L_1) - H(x - L_2)]C_0 \quad (5)$$

where H is the Heaviside function.

Diffusivities and Void Fractions

The aqueous diffusivity of the proteins was estimated using the Stokes-Einstein equation,

$$D = \frac{k_B T}{6\pi\eta R} \quad (6)$$

where k_B is the Boltzmann constant, T the temperature in Kelvin, η the viscosity of water at that temperature, and R is the radius of the molecule. GFP is barrel-shaped, with a radius of 12 Å, and a length of 42 Å (Ref. 28). A sphere of the same volume would have a radius of 16.6 Å and this is the effective Stokes radius measured experimentally.⁷ The Stokes-Einstein diffusivity is $1.98 \times 10^{-6} \text{ cm}^2/\text{s}$. This value was compared with that obtained from an empirical correlation,⁶ which relates the diffusivity at 23°C to the molecular weight,

$$D_{\text{aq},23^\circ\text{C}} = 3.6 \cdot 10^{-5} (MW)^{-0.34} \quad (7)$$

This gives $1.12 \times 10^{-6} \text{ cm}^2/\text{s}$; adjusting the values above to 23°C gives $1.4 \times 10^{-6} \text{ cm}^2/\text{s}$, a reasonable agreement.

These aqueous diffusivities apply in the episcleral potential space into which the molecules are injected, however the extracellular matrix of the other regions of the eye presents a physical barrier to movement. The sclera is a largely acellular tissue, and a fiber matrix model was shown previously to predict the diffusivity of molecules through it¹⁰. The volume of the tissue which is not occupied by exclusionary collagen fibrils is approximately 80% and the predicted diffusivity of GFP is $3.9 \times 10^{-7} \text{ cm}^2/\text{s}$ (Ref. 10). The effective diffusivities of macromolecules in the sclera have also been measured in several species. Inulin, with a molecular radius slightly smaller than GFP, was reported to have a diffusivity through the bovine sclera of $1-2 \times 10^{-7} \text{ cm}^2/\text{s}$ at 37°C (Ref. 21). Rabbit sclera demonstrated a good exponential fit of diffusivity to

molecular radius, predicting GFP diffusivity of $5.6 \times 10^{-7} \text{ cm}^2/\text{s}$ at 37°C (Ref. 2). For human, the predicted scleral diffusivity is $4 \times 10^{-7} \text{ cm}^2/\text{s}$ (Ref. 26). Thus, the predicted GFP diffusivity is in agreement with the experimental data.

The diffusivity of GFP in the other layers of the eye is estimated based on the scleral diffusivity and the extracellular fractions of the layers. It has been shown¹¹ that the diffusivities in two tissues can be related by their void fractions:

$$D_a = D_b \frac{\phi_a 3 - \phi_b}{\phi_b 3 - \phi_a} \quad (8)$$

Rabbit retina intercellular space has been measured at 30–33% total volume by inulin and electrolyte measurements;⁴ for chick retina the figure is 27%, based on inulin and sucrose measurements.⁹ We use 30% in this model, giving a retinal diffusivity value of 30% of the scleral value. The choroid is a partially cellular, partially fibrous region, and we assume that its void volume is intermediate between the sclera and retina, 40%; this gives 42% of scleral diffusivity. The periocular space is comprised of skeletal muscle and connective tissue. Skeletal muscle in the rat has been found to have interstitial volumes of 9.3–14% (Ref. 18,35); for mice, 15–20% (Ref. 20). We choose the high end of this range (20%) to include the connective tissue.

RPE, ILM and ESB Resistances

Transport of macromolecules across these barriers provides an estimate of their permeability, the inverse of transport resistance. The permeability of a monolayer of cultured RPE in retinal conditioned medium to horseradish peroxidase, a 35 kDa protein of molecular radius 30 Å, was measured at $5 \times 10^{-8} \text{ cm/s}$ (Ref. 5), giving a resistance of $2 \times 10^7 \text{ s/cm}$. Resistance to inulin, a 5 kDa polysaccharide of 14 Å radius, was $7 \times 10^4 \text{ s/cm}$. Assuming an exponential fit of permeability to radius, this predicts an RPE resistance to GFP of $1.75 \times 10^5 \text{ s/cm}$. This is close to the measured $5 \times 10^5 \text{ s/cm}$ resistance to a 22 kDa protein of a monolayer of human alveolar epithelial cells *in vitro*.³⁴ Resistance of Bruch's membrane to larger serum proteins was found to be significantly less than this figure (1–2 orders of magnitude) in eye-healthy adults,²² so its effect is neglected here as a resistance in series. As mentioned earlier, no estimates of ILM resistance are available, but it has been observed to permit movement of molecules of comparable size to GFP though not molecules over 70 kDa (Ref. 19,23). Therefore, our first estimate for the ILM is zero resistance. A possible barrier at the episcleral surface has not been demonstrated previously, and we begin with an assumption of zero for this resistance also. *In vivo* values

of RPE, ILM and ESB resistances to GFP are estimated in this paper from experimental results.

Clearance

Significant clearance is assumed to take place in only two of the layers: the periocular tissue and the choroid. The other layers have zero clearance. The episcleral space and sclera are avascular, while the blood-retinal barrier is assumed to be unaffected by GFP, preventing significant clearance of GFP from the retina. The clearance from the combined rabbit choroid and retina of FITC-conjugated IgG has been measured³, and was found to have a half-life of approximately 3 days, or a clearance rate of $2.7 \times 10^{-6} \text{ s}^{-1}$. GFP is a significantly smaller molecule, however, and the loss of GFP from the mouse choroid and retina is observed to be faster – by 4 h there is no significant remaining GFP detectable (Fig. 2a). The values of the clearance rate of GFP from the mouse eye are estimated from experimental results and discussed in the Results section. Note that GFP can also be lost across the ILM to the vitreous, governed by the resistance of the ILM. To find a baseline for the choroidal clearance, we fit the experimentally measured decline in concentration to a first order rate (exponential decay) and find that the rate constant of the clearance in each of the three layers is $3\text{--}4 \times 10^{-4} \text{ s}^{-1}$. If we run the model with this clearance rate in each of the layers, then we get clearance in the same time frame as experimentally observed; however clearance should only occur in the choroid and in the orbital tissue. If the choroid clears material from the sclera, choroid and retina (a total volume 14 times larger than choroid alone), the predicted clearance rate would need to be $4\text{--}5.5 \times 10^{-3} \text{ s}^{-1}$. If it is also responsible for clearing material from half of the potential space, this gives us a baseline for the choroidal clearance rate of $7\text{--}9 \times 10^{-3} \text{ s}^{-1}$. The vasculature of the periocular tissue also contributes to clearance, although it is unclear to what extent. We begin with an assumption of the same clearance rate from the periocular tissue.

Convection

The convection rate in the layers of the normal eye was shown to be at least 20-fold lower than the rate of diffusion¹² and is thus neglected in this analysis.

Model Solution

The equations are solved numerically, using a fully implicit finite difference scheme. A time step and spatial grid size were chosen such that increasing the

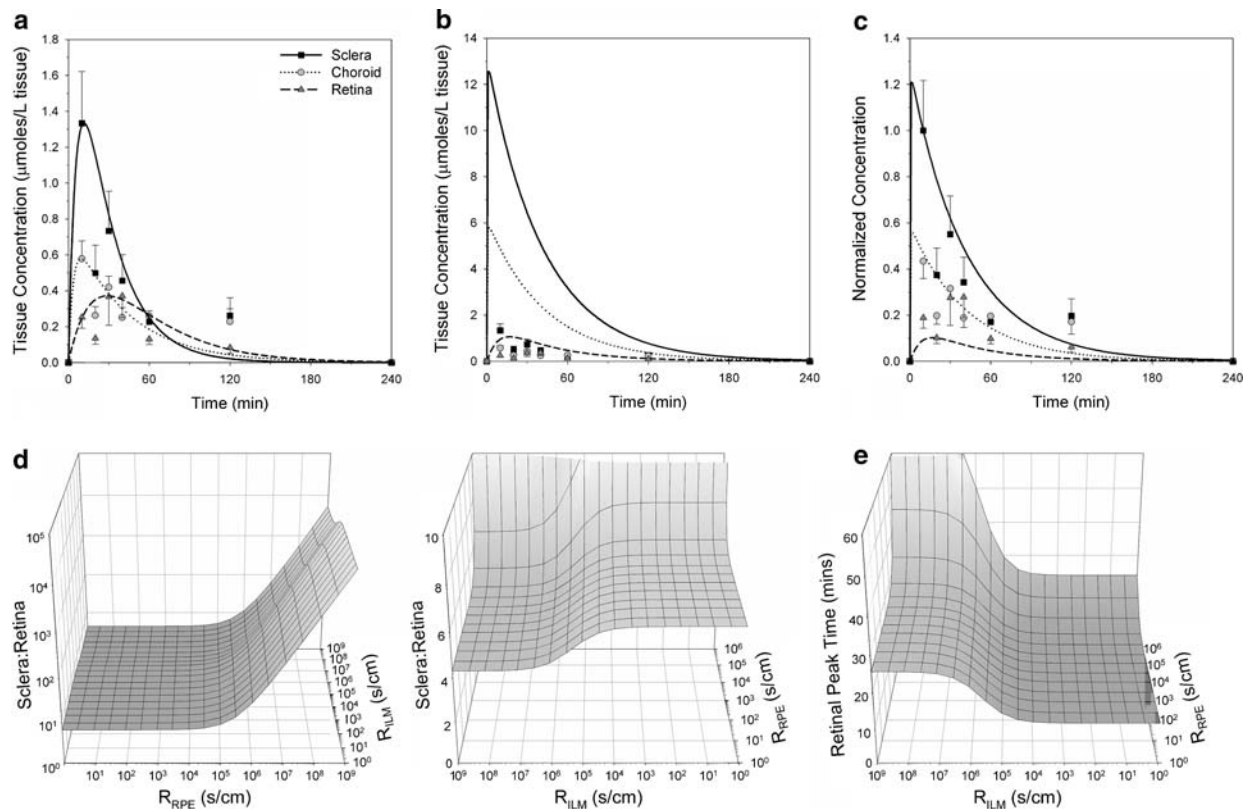


FIGURE 2. Experimental results and initial model predictions. **a**, Experimental measurements of GFP concentration in sclera, choroid and retina 10 min–4 h post injection (data from material to be published elsewhere (A.M. Demetriades *et al.*, unpublished observations)). The measured concentration is lower than the actual interstitial concentration of GFP due to incomplete global coverage of the injected solution and the void volumes (interstitial spaces) of each layer (see text). **b**, Model predictions (*lines*) for the experimental measurements for baseline values of the parameters obtained from *in vitro* experimental literature. The experimentally observed values (*symbols*) are also shown. **c**, As for **b**, but the concentrations are normalized to the concentration in the sclera at 10 min. **d**, Ratio of model-predicted scleral concentration at 10 min to predicted retinal peak concentration, as R_{RPE} and R_{ILM} are varied. All other parameters from the baseline model are held constant. **e**, Model-predicted time to reach peak concentration in the retina, as R_{RPE} and R_{ILM} are varied. All other parameters from the baseline model are held constant.

number of grid-points or decreasing the time step size did not significantly affect the results. The fractional accuracy achieved was better than 10^{-5} .

Parameter Fitting

To find parameters fitting the experimental results, a Levenberg–Marquardt method was employed. The chi-squared statistic was the sum of squares of each time point weighted by the standard error of the experimental measurements. Five parameters – three resistances and two clearance rates – are found from the experimental data. This is too many to try to fit simultaneously without inspecting the data to find limits on the parameters. Restrictive ranges for two of the resistances were obtained by inspection of the model results (see Results). Then, the Levenberg–Marquardt method was employed to find the clearance rates that best fit the data for any given value of the third resistance. The resistance that gives the best

fit to the data, and the corresponding clearance rates, were taken from these results.

RESULTS

Model Geometry: Experimental Measurements of Sclera, Choroid and Retina Thickness in the Mouse

The sclera ranged in thickness from $9.7 \mu\text{m}$ at the equator of the eye to $20.1 \mu\text{m}$ adjacent to the optic nerve (Table 1). The thickness of the choroid was also greater in the posterior portion of the eye ranging from $14.4 \mu\text{m}$ at the equator to $19.4 \mu\text{m}$ adjacent to the optic nerve. The weighted average scleral thickness used in the model was $15 \mu\text{m}$; average choroidal thickness used was $17 \mu\text{m}$. Retinal thickness was $209 \pm 5 \mu\text{m}$ ($n = 12$) by OCT measurements and was $213 \pm 9 \mu\text{m}$ ($n = 12$) by image analysis of histological sections, and therefore a value of $210 \mu\text{m}$ was used for the model. Note that the thickness of the human retina,

TABLE 1. Experimentally measured thickness of mouse sclera, choroid and retina.

Scleral thickness (μm)		
Equator of eye	9.7 ± 0.36	($n = 5$)*
1/3 of the distance from equator to optic nerve	12.9 ± 0.89	($n = 5$)
2/3 of the distance from equator to optic nerve	16.0 ± 1.01	($n = 4$)
Adjacent to optic nerve	20.1 ± 0.69	($n = 5$)
RPE/Choroid thickness (μm)		
Equator of eye	14.4 ± 0.33	($n = 5$)
$\frac{1}{2}$ of the distance from the equator to the optic nerve	16.8 ± 0.38	($n = 5$)
Adjacent to the optic nerve	19.4 ± 0.66	($n = 5$)
Retinal thickness (OCT method) (μm)		
Average	209 ± 4.8	($n = 12$)
Retinal thickness (Histology method) (μm)		
Average thickness of retina within 0.57 mm of optic disc edge	213 ± 9.3	($n = 12$)

*n is the number of eyes used in the measurement; each eye provided 3–16 measurements of different segments at each location.

246 μm (Ref. 1) is only slightly greater than that of the mouse. The thickness of human sclera varies from 390 μm near the equator to 530 μm at the limbus and 900 μm near the optic nerve²⁵. We used 600 μm as an estimate for mean thickness. The thickness of the human choroid decreases with age (from 193.5 to 84 μm)³⁰; we assumed a thickness of 200 μm . The geometric parameters used in the simulations are summarized in Table 2.

Comparison of Model Predictions with Empirical Observations

The measured concentrations of GFP in the sclera, choroid and retina are shown in Fig. 2a. The experimental data for each layer has been used to create an approximate time-dependent concentration profile for that layer by using a Levenberg–Marquardt method to fit the difference of two exponentials (which reproduces the shape of the GFP concentration profiles, Fig. 2a). There are several important metrics that can be obtained from the experimental data. The time to peak sclera and choroid concentrations are both less than or close to 10 min. The retinal peak time is between 30 and 40 min. The peak retinal concentration is approximately 0.372 $\mu\text{moles/l}$ tissue. Because the peak sclera and choroid concentrations may be greater than those measured experimentally (if the peak is earlier

than 10 min), we use the measured concentration at 10 min to compare to the model predictions at 10 min.

Model Results for Baseline Parameter Values

The simulation was run for the baseline parameters given in Table 3, representing in vitro measured and estimated values. Results are plotted as tissue concentrations (moles/l tissue) (Fig. 2b) and concentrations normalized to the 10-min scleral concentration (Fig. 2c). The predicted concentration in each layer (sclera, choroid and retina) is significantly higher than the measured concentration. Increasing the clearance rates cannot decrease the concentration sufficiently in the sclera to explain this discrepancy (data not shown). Instead, there must be a resistance at the entry point to the sclera (R_{ESB}), which will have the dual effects of lowering concentrations and delaying the time at which the peak concentrations are reached. The value of this resistance will be dealt with below.

Barrier Resistances – RPE and ILM

In addition, on the plot of normalized concentration (Fig. 2c), we can see that the predicted ratio of peak scleral concentration to peak retinal concentration exceeds the ratio measured experimentally (3.58).

TABLE 2. Thicknesses of layers in human and mouse eyes used in simulations.

	Mouse	Human
Diameter (mm)	3	25
Periocular Muscles (μm)	500	500
Sclera (μm)	15	600
Choroid (μm)	17	300
Retina (μm)	210	246

TABLE 3. Transport parameters for the model.

	Baseline	Best fit
R_{ESB} (s/cm)	0	9×10^5
R_{RPE} (s/cm)	1.75×10^5	$<10^4$
R_{ILM} (s/cm)	0	10^7
$k_{\text{cl,PO}}$ (s^{-1})	9×10^{-3}	1.6×10^{-1}
$k_{\text{cl,C}}$ (s^{-1})	9×10^{-3}	3.5×10^{-3}

This ratio is controlled by the RPE and ILM resistances (R_{RPE} and R_{ILM}) and by the choroidal clearance ($k_{cl,C}$): as RPE resistance or choroidal clearance increases, less GFP reaches the retina; as ILM resistance increases, less GFP is lost to the vitreous, allowing buildup of GFP in the retina. We will deal with the values of the clearance rates below. The model predictions for the sclera:retina concentration ratio for a range of RPE and ILM resistances is shown in Fig. 2d. Below an RPE resistance of 10^4 s/cm, the ratio is in the range 4–6. As the RPE resistance increases above 10^4 s/cm, the ratio increases quickly as GFP is blocked from the retina. This is true for all values of R_{ESB} and clearance rates tested (data not shown), and so the maximal value of RPE resistance for GFP appears to be 10^4 s/cm. We will show later that values of RPE resistance below 10^4 s/cm do not substantially alter the results of the model, or agreement with experiment. Looking more closely at the low- R_{RPE} region, we observe that there are two subregions – high ILM resistance and low ILM resistance. At low R_{ILM} – less than 10^5 s/cm – GFP moves through the ILM and into the vitreous. At high R_{ILM} – 10^7 s/cm and higher – the barrier formed by the ILM causes GFP to build up in the retina and the sclera:retina ratio to decline (to approximately 4, close to the experimental value). Again, this is true for all R_{ESB} and clearance rates tested. Using another metric, the time to peak retinal concentration (Fig. 2e), the experimental value for GFP is between 30 and 40 min. Here again, the combination of low R_{RPE} and high R_{ILM} gives a model prediction of retinal peak time in good agreement with experiment. Thus, we estimate the values of R_{RPE} and R_{ILM} to be less than 10^4 s/cm and greater than 10^7 s/cm, respectively.

Episcleral Resistance and Clearance Rates

Using the calculated values of R_{RPE} and R_{ILM} , three undetermined parameters remain: episcleral resistance (R_{ESB}) and the clearance rates from the periorcular tissue and choroid ($k_{cl,PO}$ and $k_{cl,C}$). Starting with a range of R_{ESB} values, we used an optimization method (the Levenberg-Marquardt method) to find the clearance rates which best fit the model to the experimental results. The resulting best-fit peak concentrations (Fig. 3a) and time to peak (Fig. 3b) for sclera, choroid and retina are R_{ESB} -dependent. The concentrations are close to the experimental values for R_{ESB} values close to 10^6 s/cm. Similarly, the time to peak scleral and choroidal concentration (approximately 10 min) and retinal concentration (30–40 min) is in agreement with experiment for R_{ESB} values of approximately 10^6 s/cm. The value of R_{ESB} which gives the closest fit to the peak sclera concentration is 9×10^5 s/cm. We use this value for R_{ESB} for GFP in the following work. Increased R_{ESB} beyond this value gives decreasing concentrations of GFP in the eye; decreased R_{ESB} decreased the time to peak retinal concentration. The clearance rates which give the best fit at this R_{ESB} are $1.6 \times 10^{-1} \text{ s}^{-1}$ and $3.5 \times 10^{-3} \text{ s}^{-1}$ for periorcular and choroidal clearance, respectively. As a check that the resistances found earlier are still valid, we note that the high ILM resistance and low RPE resistance is again the regime which gives sclera:retina concentration ratio and time to retinal peak close to experiment.

Interstitial Concentration of GFP

The values of the transport parameters found by fitting the experimental data are given in Table 3. The model predictions for the tissue concentrations of GFP in sclera, choroid and retina are shown in Fig. 4a. The

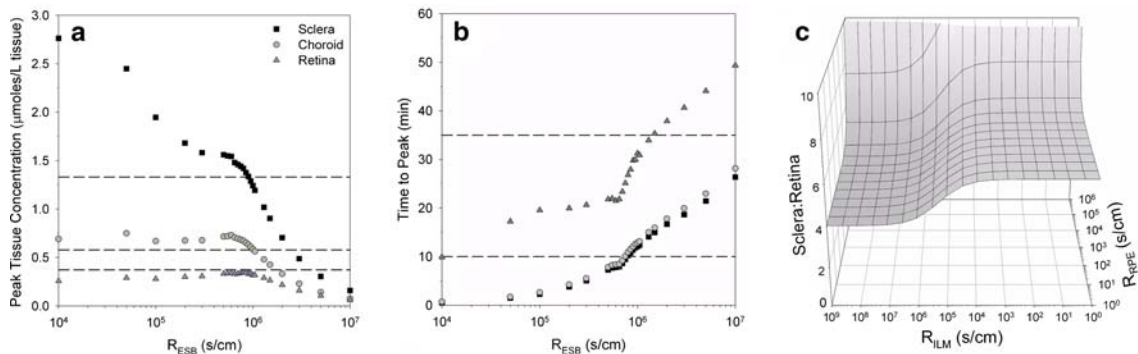


FIGURE 3. Best fit of barrier resistances and clearances. a, Model predictions (*symbols*) of peak tissue concentrations of GFP; best fit to the experimental measurements for increasing values of R_{ESB} . At each value of R_{ESB} , a Levenburg-Marquardt procedure was used to optimize the fit to the experimental data by adjusting the clearance rates. The experimentally measured values (*lines*) are shown. b, Model predictions of time to reach peak concentration of GFP, obtained as in a. Notation as in A. c, As for Fig. 2d, using best fit R_{ESB} and clearance rates (see text).

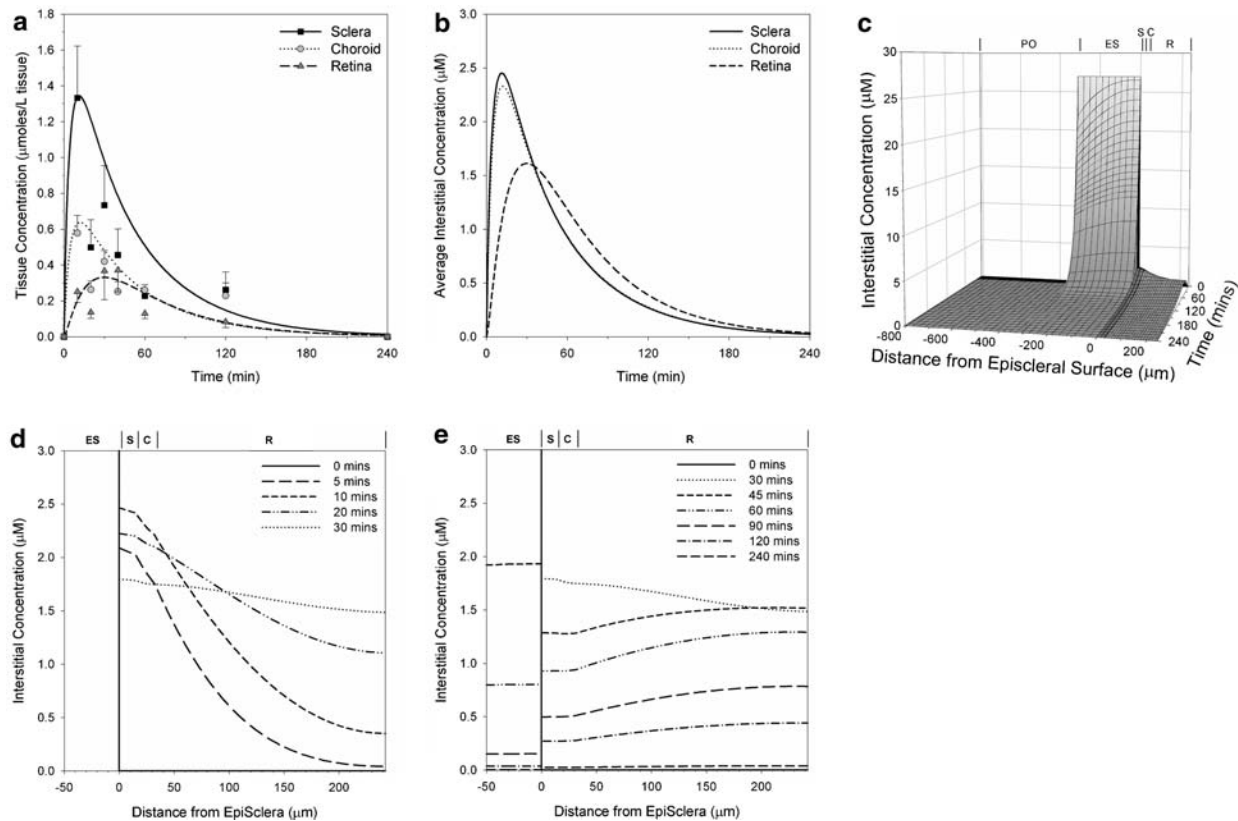


FIGURE 4. Best fit model predictions for GFP transport. **a**, Model predictions (*lines*) for the experimental measurements for best fit values of the parameters (see text). The experimentally observed values (*symbols*) are also shown. **b**, Average interstitial concentration of GFP in the sclera, choroid and retina. **c**, Interstitial concentration across the eye. PO, periocular tissue; ES, episcleral space; S, sclera; C, choroid; R, retina. **d** and **e**, Interstitial concentration profile in sclera, choroid and retina at 5 min–4 h. Notation as in **c**.

tissue concentration is the one that is measured experimentally; however, the concentration of GFP which would be sensed by the cells in the choroid and retina is the interstitial one, which as discussed earlier is different from the tissue concentration. The spatially averaged interstitial concentrations (Fig. 4b) of the sclera and choroid are almost identical; this is expected since the sclera and choroid are thin and are not separated by a significant resistance. Even though there is clearance from the choroid, the concentration quickly equilibrates between these two thin compartments. The peak choroid concentration, $2.3 \mu\text{M}$, is approximately 8.6% of the concentration of the injected solution. The peak retina concentration, $1.7 \mu\text{M}$ is 6.2% of the injected GFP concentration. We note also that the concentration in the retina is higher than that in the sclera and choroid after 35 min. This is due to the high ILM resistance, allowing the buildup of GFP in the retina, which gradually returns to the choroid to be cleared. This is illustrated more clearly by looking at the interstitial concentration of GFP across the layers of the eye (Fig. 4c). The sclera, choroid and retina concentration profiles are shown in more detail in Fig. 4d.

The concentration in the retina rises until 30 min, and then begins to decline; the concentration in the choroid and sclera declines more quickly due to the clearance from the choroid, and thus the concentration gradient reverses.

Clearance of GFP from the Eye

The concentration of GFP in the episcleral potential space declines quickly and after 75 min only 1% of the injected material remains in the space (Fig. 5a). An exponential curve fit to this result has the first order rate constant $8 \times 10^{-4} \text{ s}^{-1}$. The fate of the GFP which enters the layers of the eye is shown in Fig. 5b. 99% of the GFP is cleared from the eye or lost to the vitreous by 95 min. Only 0.1% of the material is lost to the vitreous (due to the high ILM resistance).

Parameter Sensitivity

To investigate the sensitivity of these results to the parameters of the model, we conducted simulations

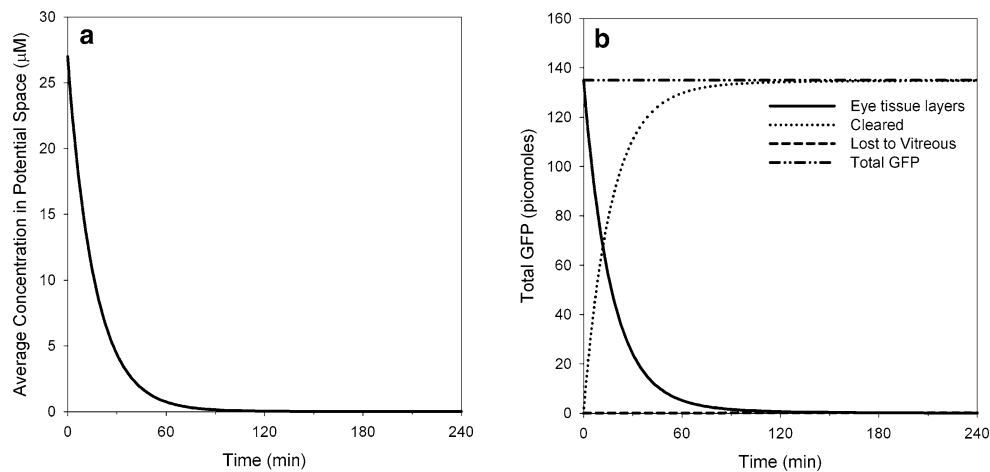


FIGURE 5. Clearance of GFP from the eye. a, Depletion of GFP from the episcleral potential space. b, Fate of GFP: protein remaining in the layers of the eye, lost to clearance, and lost to vitreous.

varying each of the parameters individually and plotted the resulting changes to peak concentration, peak time and total integrated concentration (over 4 h) in both choroid and retina (Fig. 6). Scleral metrics are not included as these would be indistinguishable from the choroidal metrics due to the thinness of the layers and the lack of a significant barrier resistance between them. As an example, a decrease in the ILM resistance does not affect choroidal peak concentration, but does lower the total amount of GFP in the choroid over 4 h (Fig. 6a); the ILM resistance has a more direct effect on the metrics of the retina, increasing both peak concentration and the time required to reach that peak. The results are summarized in Table 4.

Larger Molecules

Molecules larger than GFP may be used as anti-angiogenic agents in the eye. The effect of increasing size on protein transport may be assessed using the parameter sensitivity (Fig. 6). Increasing molecular radius will lead to increased resistances, decreased clearance rates and decreased diffusivity. These lead to, respectively: decreased protein entry to the sclera and retina (but increased retention in the retina by the ILM) (Fig. 6a); decrease in the loss of protein to clearance and thus retention in the eye (Fig. 6b); and slightly increased protein retention (Fig. 6c). The effect on choroidal and retinal delivery is difficult to predict without repeating the model simulations with

all of these parameters changed to reflect the transport characteristics of that specific molecule, thus more work is required to understand the *in vivo* variation in clearance rates and resistances with molecular size.

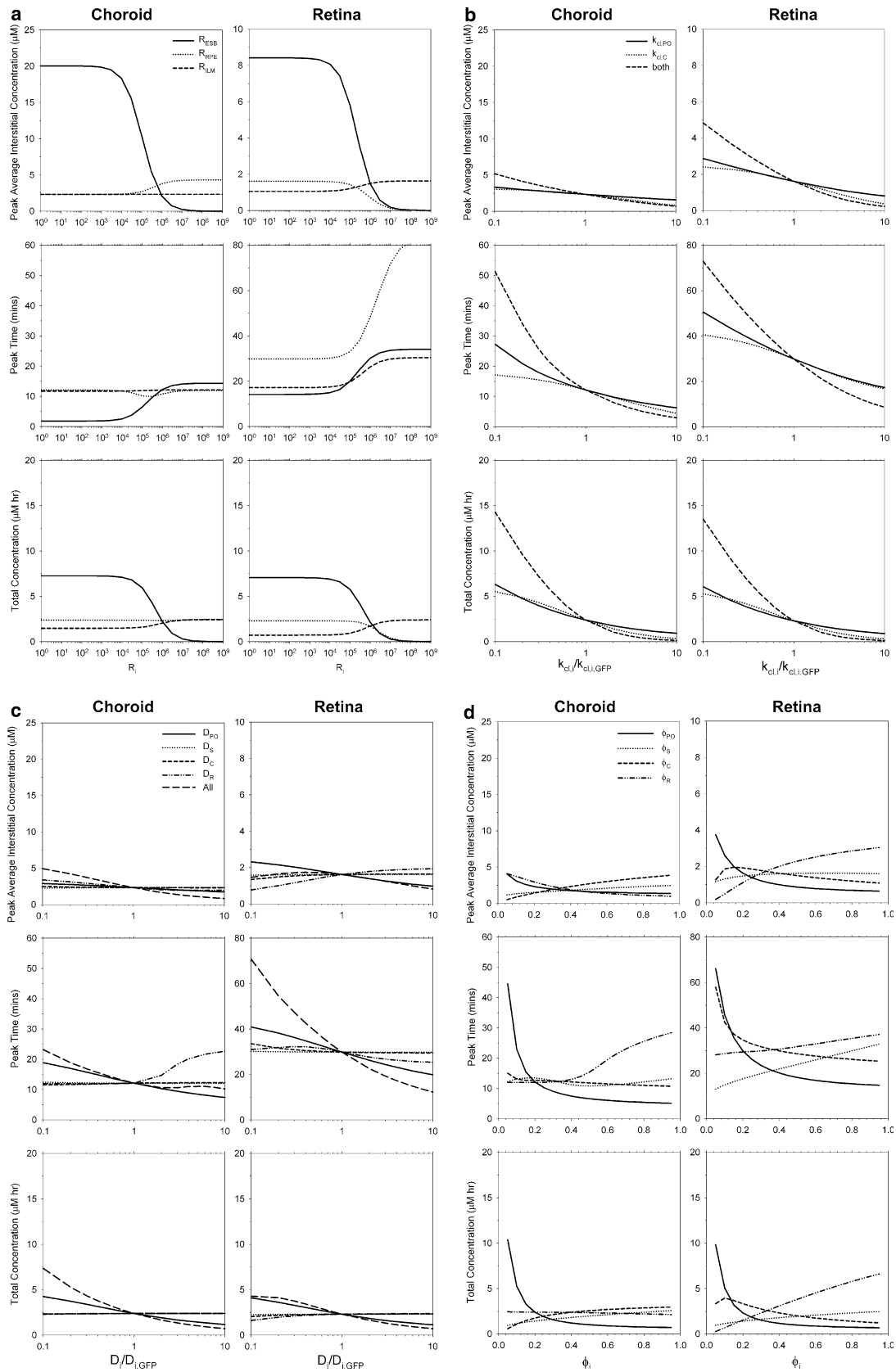
Increasing Drug Delivery to the Choroid and Retina

For delivery of anti-angiogenic molecules, the major goal is to increase the delivery of protein to the choroid and retina. One way would be to decrease the episcleral resistance (Fig. 6a), allowing more of the injected protein to enter the sclera. However, the model reveals that the most effective way would be to decrease the clearance rates from the eye (Fig. 6b). A 10-fold change in the clearance rates can double the peak retinal concentration. Note that the ILM and RPE resistances found in our simulations are in the optimum ranges for increased concentration in the retina; but if the target is choroidal neovascularization, a higher RPE resistance would improve delivery to that layer (Fig. 6a). Diffusivity changes do not increase the overall delivery significantly (Fig. 6c).

Intravitreal Injection

Intravitreal injection, an alternative route of delivery to the retina for proteins, that can penetrate the ILM, was investigated using the same theoretical model and the parameters obtained from this study. In

FIGURE 6. Parameter sensitivity. a, Variation in barrier resistances. Peak average interstitial concentration, time to reach peak and integrated total concentration in the choroid and retina. Each resistance is varied independently as the others are held at the values used in Figs. 4 and 5. b, Variation in clearance rates. Graphs as in a. c, Variation in diffusivities. Graphs as in a. d, Variation in void volumes. Graphs as in a.



this case, we assume a vitreous with a high diffusivity and at least 200 μm thick (increasing the size of the vitreous does not significantly affect the results over the 4 h time period studied). The initial concentration in the vitreous is assumed to be the same as the initial concentration in the periocular injection solution (27 μM). This requires more GFP as the volume of the vitreous is larger than the injection volume. The results of this simulation are shown in Fig. 7. For an assumed GFP clearance rate from the vitreous of 10^{-4} s^{-1} (less than the aqueous turnover rate¹², but significantly faster than the clearance rate for monoclonal antibodies^{23,24}), the peak interstitial concentration in the retina is 0.75 μM (Fig. 7a), less than half that achieved by periocular injection (Fig. 4b); however, the concentration stays high longer, as the GFP in the vitreous is cleared slowly. Delivery to the choroid is even less – 0.4 μM is the peak concentration compared to 2.3 μM by periocular injection (Fig. 4b). The concentration across the layers of the eye is shown in Fig. 7b; note the slower clearance of GFP from the vitreous relative to the loss from the episcleral space (Figs. 4c, 5a); almost none of the intravitreal GFP reaches the periocular tissues (Fig. 7c). We repeated this simulation with zero clearance in the vitreous, and a peak retinal and choroidal concentrations of 1.2 μM and .65 μM were reached (Fig. 7d); because of the lack of clearance, these concentrations were maintained long past 4 h. It is clear, then, that to model the results of intravitreal injection correctly, we need the clearance rate of GFP from the vitreous.

Simulated Injection into Human Eye

To understand how drug delivery by periocular injection to the human eye would function, we scaled up our model geometry to more closely approximate the human eye (Table 2). Barrier resistances, diffusivities, and clearance rates were maintained; only the thicknesses of the layers were assumed to change from the mouse. This gives us an initial estimate of the resistances faced by protein in the episcleral space (Fig. 8a). Note that the resistance due to the sclera and choroid are significantly higher in human eyes due to the increase in thickness, whereas the retina, which is only slightly thicker in humans, does not pose a significant increase in resistance. The resulting peak interstitial concentrations are significantly lower than in the mouse for an injection of the same concentration of GFP in a volume (0.35 ml) which gives the same thickness of episcleral space as in the mouse (Figs. 8b, 4b). However, this is not the correct scaling for the total GFP dose (70-fold increase in volume and total dose) from mouse to human. Because this is local administration of drug, draft FDA guidelines (<http://www.fda.gov/cder/guidance/3814dft.pdf>) suggest that the ‘drug’ (GFP in this case) dose be scaled to a local geometric parameter. If we choose this to be retinal thickness, then the results are not significantly different from Fig. 8b; however if we choose choroidal thickness, which is 12-fold larger in human than in mouse, then the thickness of the episcleral layer must be increased by the same factor, which

TABLE 4. Parameter sensitivity.

Parameter	Peak Concentration*				Time to Peak*				Total Concentration*			
	Choroid		Retina		Choroid		Retina		Choroid		Retina	
	↓	↑	↓	↑	↓	↑	↓	↑	↓	↑	↓	↑
R_{ESB}	4.91	-8.85	3.92	-8.42	-1.90	1.15	-1.51	1.11	2.68	-7.34	2.69	-7.36
R_{RPE}	-1.00	1.00	1.00	-1.00	1.00	1.00	1.00	1.00	1.00	-1.00	1.00	-1.00
R_{ILM}	-1.00	1.00	-1.08	1.01	-1.00	1.00	-1.13	1.02	-1.16	1.02	-1.33	1.04
$k_{\text{cl,PO}}$	1.42	-1.48	1.78	-2.01	2.25	-1.94	1.69	-1.73	2.66	-2.57	2.64	-2.56
$k_{\text{cl,C}}$	1.30	-2.91	1.49	-4.38	1.41	-2.75	1.36	-1.79	2.33	-7.09	2.30	-7.54
D_{PO}	1.24	-1.33	1.43	-1.67	1.56	-1.64	1.37	-1.50	1.79	-2.03	1.78	-2.03
D_{S}	-1.03	1.00	-1.03	1.00	1.02	-1.00	1.11	-1.00	-1.02	1.00	-1.02	1.00
D_{C}	1.07	-1.01	-1.21	1.02	-1.05	1.02	1.12	-1.01	-1.04	1.00	-1.12	1.01
D_{R}	1.45	-1.19	-2.12	1.20	-1.01	1.87	1.04	-1.18	-1.01	1.00	-1.43	1.03
ϕ_{PO}	1.33	-1.18	1.61	-1.34	1.88	-1.35	1.53	-1.27	2.20	-1.53	2.19	-1.53
ϕ_{S}	-1.05	1.04	1.00	-1.01	-1.05	1.06	-1.07	1.07	-1.06	1.05	-1.05	1.04
ϕ_{C}	-1.22	1.16	1.09	-1.09	1.03	-1.03	1.06	-1.05	-1.12	1.07	1.19	-1.16
ϕ_{R}	1.27	-1.24	-1.46	1.24	-1.02	1.07	-1.01	1.03	1.01	-1.01	-1.53	1.33

*Fold change in metrics due to 10-fold (or 10% for ϕ) change in parameters from best-fit values. Positive numbers, fold increase; negative numbers, fold decrease; 1.00 represents no change.

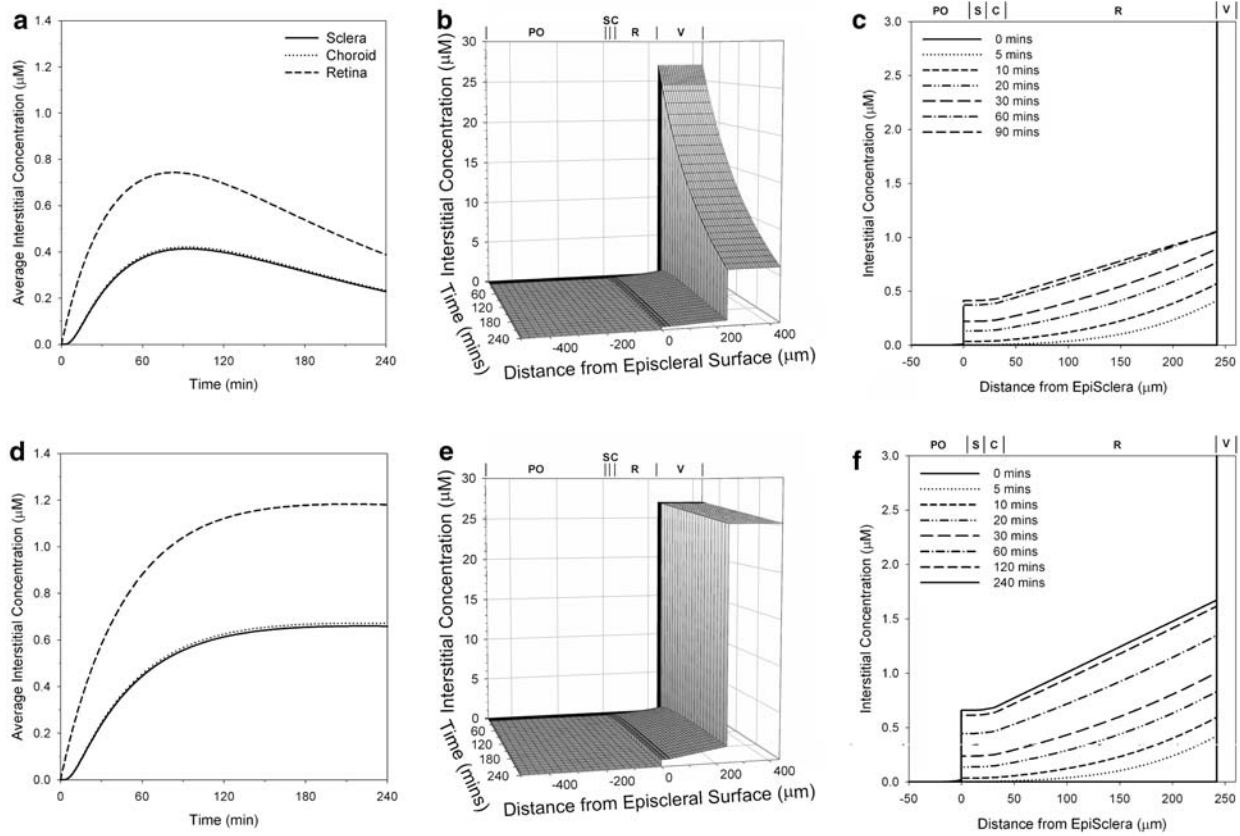


FIGURE 7. Intravitreal injection. a, Average interstitial concentration in sclera, choroid and retina, following intravitreal injection to same final concentration ($27 \mu\text{M}$). All transport values as for Figs. 4–5, plus a vitreous clearance rate of 10^{-4} s^{-1} . b, Interstitial concentration across the eye. PO, periocular tissue; S, sclera; C, choroid; R, retina; V, vitreous. c, Interstitial concentration profile in sclera, choroid and retina at 5 min–4 h. Notation as in b. d–f, As for a–c, with zero vitreous clearance rate.

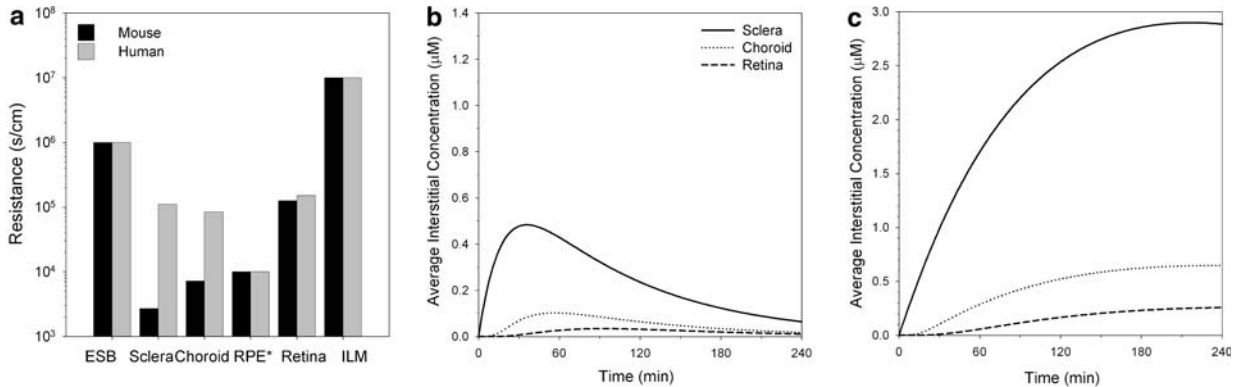


FIGURE 8. Human scale-up. a, Resistances of the layers and intralayer barriers in the mouse and human eye. ESB, EpiScleral Barrier; RPE, Retinal Pigmented Epithelium; ILM, Internal Limiting Membrane. b, Model prediction of average interstitial concentration in the sclera, choroid and retina following injection of same concentration of GFP into periocular space of human eye. c, As for b, with volume of injection increased in proportion to increase in choroidal volume.

leads to a higher and more sustained peak scleral concentration (Fig. 8c); however, the choroidal and retinal peak concentrations are still lower than those observed in the mouse.

DISCUSSION

We have developed a model to simulate the transport of proteins through the layers of the eye following

periocular or intravitreal injections. This model was used to characterize the transport parameters of GFP through the mouse eye using *in vivo* experimental data on GFP concentration in each layer of the eye at several timepoints following periocular injection. Using these transport parameters, we can make predictions for the transport of GFP following intravitreal injection, as well as predictions for how GFP would be transported in the human eye.

We note that the resistance of the retinal pigmented epithelium (RPE) to GFP estimated by the model is, unexpectedly, at least two orders of magnitude lower than that predicted by *in vitro* cell culture models of RPE cells^{5,15}, or by *in vitro* experiments of transport across explanted RPE-choroid layers²⁹. It is possible that the *in vivo* microenvironment, e.g. presence of other layers and other cell types, results in increased permeability of the RPE layer *in vivo* relative to the measured protein permeability of an RPE cell monolayer *in vitro*. Alternatively, there may be facilitated transport, e.g. a vesicular pathway, aiding the movement of GFP across the RPE barrier. Since GFP is not normally found in the mouse, it would be unlikely to be a specific transport route, and thus this process may apply to other proteins delivered to the eye. This facilitated transport may take place in one direction only (i.e. from the choroid into the retina), although in this model we have assumed that the transport resistances are the same in each direction. If there is directionality to the transport barriers then experimental results for intravitreal injections (i.e. average movement in the opposite direction) will be different from those predicted in Fig. 7. We also make the distinction between transscleral transport, such as the route of GFP movement, and transvascular transport such as that used by fluorescein angiography, which we do not study here. Larger molecules than GFP may also experience a higher resistance at the RPE. However, this is the first measurement of RPE resistance for an RPE layer *in situ* in the eye, by measuring the concentration of a protein in the layers on each side of the barrier. Revealing the discrepancy between our *in vivo* results of RPE permeability to GFP and the *in vitro* measurements of RPE explant or RPE cell culture monolayer permeability is an important result of our studies. It is also an example of the power and utility of computational models in providing insight into *in vivo* transport processes.

The other resistances in this model, at the episcleral barrier (ESB) and at the internal limiting membrane (ILM), were surprisingly high for a protein of moderate molecular weight such as GFP. The ILM has the physical characteristics of a basement membrane, but we do not know the structure or thickness of the bar-

rier at the episclera. However, these resistances are not outside the range of reasonable values for thin layers of large extracellular molecules. The glycocalyx of endothelial cells, a cell-surface associated layer of proteoglycans with their associated glycosaminoglycan chains, is estimated to be less than 500 nm thick, and yet exhibits resistances in the range 10^6 – 10^8 s/cm for molecules of molecular radius 15–50 Å (Ref. 32). Thus the ESB resistance could arise from a layer which is difficult to see on micrographs. The ESB resistance is predicted to be 10-fold less than the ILM resistance for GFP, and this gives rise to the predicted differences in retinal and choroidal drug delivery following periocular and intravitreal injections (Figs. 4, 7). In addition, the ESB resistance determined using the model may be an overestimate as the model assumes that the injection site is at the episcleral surface. In practice, the fluid may be injected a short distance away, introducing a diffusive barrier between the injection site and the episcleral surface and decreasing the effective concentration at the surface. This could significantly decrease the R_{ESB} required by the model to fit the experimental results.

GFP is not an angiogenic or anti-angiogenic agent, but it is a nonbinding nonreactive protein which serves as a test protein to measure transport through the eye. It was chosen because it is assumed to be inert and unexpressed in the normal eye. However, this transport model should be tested with endogenously expressed proteins, to test whether the atypical protein (i.e. GFP) behaves differently. The model should also be tested for proteins that prevent or regress choroidal and retinal neovascularization, e.g. PEDF, soluble VEGF receptors and antibodies. All of these are larger than GFP, and thus the transport parameters may be different: higher diffusivities, lower clearance rates, and higher resistances. The RPE, for example, appears to be a more significant barrier to PEDF transport than it is for GFP (A.M. Demetriades and P.A. Campochiaro, unpublished observations). Thus, larger molecules should be investigated in order to establish molecular size-based correlations for these *in vivo* parameters. In addition, binding by extracellular or cell-surface binding sites may be a significant sink and have an impact on transport.

The model also has potential to describe gene delivery protocols and thus model experiments involving more chronic delivery.^{13,14,33} It is possible to include source terms representing the secretion of protein from cells of the periocular or ocular tissues following transfection by the genes of interest. Sustained-release methods such as these would result in significantly different concentration profiles in the choroid and retina from the protein-injection results. Periocular injections are particularly promising for

gene transfer as intravitreal injections may result in the undesirable transfection of cells that are critical for vision.

GLOSSARY

PO	periocular tissue
ES	episcleral space
S	sclera
C	choroid
R	retina
ESB	episcleral barrier
RPE	retinal pigmented epithelium
ILM	internal limiting membrane
C	effective concentration
C_{int}	interstitial concentration
α	fractional coverage of sclera by injection
D_i	effective diffusivity of layer i
$k_{\text{cl},i}$	rate of clearance from layer i
ϕ_i	fractional void volume of layer i
L_i	thickness of layer i
R_i	resistance of barrier i

REFERENCES

- Alamouti, B. and J. Funk. Retinal thickness decreases with age: an OCT study. *Br. J. Ophthalmol.* 87:899–901, 2003.
- Ambati, J., C. S. Canakis, J. W. Miller, E. S. Gragoudas, A. Edwards, D. J. Weissgold, I. Kim, F. C. Delori, and A. P. Adamis. Diffusion of high molecular weight compounds through sclera. *Invest. Ophthalmol. Vis. Sci.* 41:1181–1185, 2000.
- Ambati, J., E. S. Gragoudas, J. W. Miller, T. T. You, K. Miyamoto, F. C. Delori, and A. P. Adamis. Transscleral delivery of bioactive protein to the choroid and retina. *Invest. Ophthalmol. Vis. Sci.* 41:1186–91, 2000.
- Ames, A. 3rd, and F. B. Nesbett. Intracellular and extracellular compartments of mammalian central nervous tissue. *J. Physiol.* 184:215–238, 1966.
- Ban, Y. and L. J. Rizzolo. A culture model of development reveals multiple properties of RPE tight junctions. *Mol. Vis.* 3:18.
- Berk, D. A., F. Yuan, M. Leunig, and R. K. Jain. Fluorescence photobleaching with spatial Fourier analysis: measurement of diffusion in light-scattering media. *Biophys. J.* 65:2428–2436, 1993.
- Busch, N. A., T. Kim, and V. A. Bloomfield. Tracer diffusion of proteins in DNA solutions. 2. Green fluorescent protein in crowded DNA solutions. *Macromolecules* 33:5932–5937, 2000.
- Campochiaro, P. A., P. Soloway, S. J. Ryan, and J. W. Miller. The pathogenesis of choroidal neovascularization in patients with age-related macular degeneration. *Mol. Vis.* 5:34.
- De Azeredo, F. A. and H. Martins-Ferreira. Changes in fluid compartments and ionic composition in the isolated chick retina during SD. *Neurochem. Res.* 4:99–107, 1979.
- Edwards, A. and M. R. Prausnitz. Fiber matrix model of sclera and corneal stroma for drug delivery to the eye. *AIChE J.* 44:214–225, 1998.
- el-Kareh, A. W., S. L. Braunstein, and T. W. Secomb. Effect of cell arrangement and interstitial volume fraction on the diffusivity of monoclonal antibodies in tissue. *Biophys. J.* 64:1638–1646, 1993.
- Ethier, C. R., M. Johnson, and J. Ruberti. Ocular biomechanics and biotransport. *Annu. Rev. Biomed. Eng.* 6:249–273, 2004.
- Gehlbach, P., A. M. Demetriades, S. Yamamoto, T. Deering, E. J. Duh, H. S. Yang, C. Cingolani, H. Lai, L. Wei, and P. A. Campochiaro. Periocular injection of an adenoviral vector encoding pigment epithelium-derived factor inhibits choroidal neovascularization. *Gene Ther.* 10:637–646, 2003.
- Gehlbach, P., A. M. Demetriades, S. Yamamoto, T. Deering, W. H. Xiao, E. J. Duh, H. S. Yang, H. Lai, I. Kovessi, M. Carrion, L. Wei, and P. A. Campochiaro. Periocular gene transfer of sFlt-1 suppresses ocular neovascularization and vascular endothelial growth factor-induced breakdown of the blood-retinal barrier. *Hum. Gene Ther.* 14:129–141, 2003.
- Geiger, R. C., C. M. Waters, D. W. Kamp, and M. R. Glucksberg. KGF prevents oxygen-mediated damage in ARPE-19 cells. *Invest. Ophthalmol. Vis. Sci.* 46:3435–3442, 2005.
- Gragoudas, E. S., A. P. Adamis, E. T. Cunningham Jr., M. Feinsod, and D. R. Guyer. Pegaptanib for neovascular age-related macular degeneration. *N. Engl. J. Med.* 351:2805–2816, 2004.
- Inomata, H. and A. Bill. Exit sites of uveoscleral flow of aqueous humor in cynomolgus monkey eyes. *Exp. Eye Res.* 25:113–118, 1977.
- Jain, R. K.. Transport of molecules in the tumor interstitium: a review. *Cancer Res.* 47:3039–3051, 1987.
- Kamei, M., K. Misono, and H. Lewis. A study of the ability of tissue plasminogen activator to diffuse into the subretinal space after intravitreal injection in rabbits. *Am. J. Ophthalmol.* 128:739–746, 1999.
- Kim, Y. R., M. D. Savellano, D. H. Savellano, R. Weissleder, and A. Bogdanov Jr. Measurement of tumor interstitial volume fraction: method and implication for drug delivery. *Magn. Reson. Med.* 52:485–494, 2004.
- Maurice, D. M. and J. Polgar. Diffusion across the sclera. *Exp. Eye Res.* 25:577–582, 1977.
- Moore, D. J. and G. M. Clover. The effect of age on the macromolecular permeability of human Bruch's membrane. *Invest. Ophthalmol. Vis. Sci.* 42:2970–2975, 2001.
- Mordenti, J., R. A. Cuthbertson, N. Ferrara, K. Thomsen, L. Berleau, V. Licko, P. C. Allen, C. R. Valverde, Y. G. Meng, D. T. Fei, K. M. Fourre, and A. M. Ryan. Comparisons of the intraocular tissue distribution, pharmacokinetics, and safety of 125I-labeled full-length and Fab antibodies in rhesus monkeys following intravitreal administration. *Toxicol. Pathol.* 27:536–544, 1999.
- Mordenti, J., K. Thomsen, V. Licko, L. Berleau, J. W. Kahn, R. A. Cuthbertson, E. T. Duenas, A. M. Ryan, C. Schofield, T. W. Berger, Y. G. Meng, and J. Cleland. Intraocular pharmacokinetics and safety of a humanized monoclonal antibody in rabbits after intravitreal administration of a solution or a PLGA microsphere formulation. *Toxicol. Sci.* 52:101–106, 1999.

- ²⁵Olsen, T. W., S. Y. Aaberg, D. H. Geroski, and H. F. Edelhauser. Human sclera: thickness and surface area. *Am. J. Ophthalmol.* 125:237–241, 1998.
- ²⁶Olsen, T. W., H. F. Edelhauser, J. I. Lim, and D. H. Geroski. Human scleral permeability. Effects of age, cryotherapy, transscleral diode laser, and surgical thinning. *Invest. Ophthalmol. Vis. Sci.* 36:1893–1903, 1995.
- ²⁷Olsen, T. W., S. Sanderson, X. Feng, and W. C. Hubbard. Porcine sclera: Thickness and surface area. *Invest. Ophthalmol. Vis. Sci.* 43:2529–2532, 2002.
- ²⁸Ormo, M., A. B. Cubitt, K. Kallio, L. A. Gross, R. Y. Tsien, and S. J. Remington. Crystal structure of the *Aequorea victoria* green fluorescent protein. *Science* 273:1392–1395, 1996.
- ²⁹Pitkanen, L., V. P. Ranta, H. Moilanen, and A. Urtti. Permeability of retinal pigment epithelium: Effects of permeant molecular weight and lipophilicity. *Invest. Ophthalmol. Vis. Sci.* 46:641–646, 2005.
- ³⁰Ramrattan, R. S., T. L. van der Schaft, C. M. Mooy, W. C. de Bruijn, P. G. Mulder, and P. T. de Jong. Morphometric analysis of Bruch's membrane, the choriocapillaris, and the choroid in aging. *Invest. Ophthalmol. Vis. Sci.* 35:2857–2864, 1994.
- ³¹Rosenfeld, P. J., N. Villate, W. J. Feuer, C. A. Puliafito, and E. R. McCluskey. RhuFab V2 (Anti-VEGF Antibody Fragment) in Neovascular AMD: Safety, tolerability, and efficacy of multiple, escalating dose intravitreal injections. *Invest. Ophthalmol. Vis. Sci.* 44 (suppl):970.
- ³²Squire, J. M., M. Chew, G. Nneji, C. Neal, J. Barry, and C. Michel. Quasi-periodic substructure in the microvessel endothelial glycocalyx: A possible explanation for molecular filtering?. *J. Struct. Biol.* 136:239–255, 2001.
- ³³Takahashi, K., Y. Saishin, R. L. Silva, Y. Oshima, S. Oshima, M. Melia, B. Paszkiet, D. Zerby, M. J. Kadan, G. Liau, M. Kaleko, S. Connelly, T. Luo, and P.A. Campochiaro. Intraocular expression of endostatin reduces VEGF-induced retinal vascular permeability, neovascularization, and retinal detachment. *FASEB J.* 17:896–898, 2003.
- ³⁴Wang, Z. and Q. Zhang. Transport of proteins and peptides across human cultured alveolar A549 cell monolayer. *Int. J. Pharm.* 269:451–456, 2004.
- ³⁵Wiig, H., M. DeCarlo, L. Sibley, and E. M. Renkin. Interstitial exclusion of albumin in rat tissues measured by a continuous infusion method. *Am. J. Physiol.* 263:H1222–1233, 1992.